Supporting Information

Joshua et al. 10.1073/pnas.1221453110

SI Text

1. Nature of the Coupling to the Magnetic Field. In the main text, we pointed out that the coupling of the applied magnetic field to the system must necessarily involve spin–orbit interactions. In this section, we expand more on the underlying reasoning.

In general, the coupling of the field could be due purely to spin, purely to orbital, or to a spin–orbit coupled system. Pure spin coupling can be ruled out immediately in our measurements because it would be independent of the direction of the in-plane field $H^{||}$ and so cannot cause anisotropic magnetoresistance (AMR). Pure orbital coupling, on the other hand, seems to nicely fit some of the observations: This coupling has a natural critical field, the field at which the magnetic length is comparable to the confinement width of the 2D electrons. Besides, the d_{XZ}/d_{YZ} wavefunctions being less confined than the d_{XY} wavefunction (they are lighter in this direction) would explain why the coupling to them is better. Furthermore, orbital coupling would differentiate between the d_{XY}/d_{YZ} bands: Because orbital coupling is inversely proportional to the band mass perpendicular to the direction of $H^{||}$, which for a general angle of the field in the plane ϕ_H is not identical for the two bands, this coupling will lift their degeneracy and will induce orbital polarization, making one Fermi ellipse larger than the other. This orbital polarization would lead to crystalline anisotropy, and if it also causes interband scattering to be suppressed, this scenario may also explain the drop in ρ_{XX}. However, despite this apparent agreement, three pieces of data exclude orbital coupling as the relevant mechanism. First, we observe that the ρ_{XX} fall occurs for all angles ϕ_H at the same value of $H^{||}$. If this drop was due to band polarization, no drop should have been observed along, e.g., $\phi_H = 45°$, where $H^{||}$ couples identically to both orbitals and does not lift their degeneracy. Second, orbital coupling cannot explain why the behavior is similar in parallel and perpendicular fields (Fig. S2; see also ref 1). Third, the sign of orbital coupling is wrong: Such coupling would increase the band mass perpendicular to the field direction, and thus ρ_{XX} will increase when the field is perpendicular to the current, whereas we measure a decrease of ρ_{XX} in this relative orientation (positive AMR). In fact, negative AMR was observed at elevated temperatures (2), suggesting that at high temperatures the width of the 2D is large and orbital effects are important. We observe the opposite sign at $T = 2$ K, clearly showing that this is not an orbital effect. Thus, the only remaining coupling mechanism is that of a field to a spin–orbit coupled system.

2. Mean-Field Theory of the t_{2g} Itinerant Bands Coupled to Localized Spins. Our starting point for the theoretical analysis is the Hamiltonian of three itinerant bands coupled to a disordered lattice of localized moments

$$\mathcal{H} = \sum_{k}\sum_{\alpha,\alpha'=1}^{3}(\epsilon_{\alpha\alpha'}(\boldsymbol{k}) - \mu\,\delta_{\alpha\alpha'})c^{+}_{\alpha\boldsymbol{k}}c_{\alpha'\boldsymbol{k}} + \mathcal{H}_{SO} + \mathcal{H}_{H} - \lambda\sum_{i} d_i^{+}d_i + J_K\sum_{i}\boldsymbol{S}_i\cdot\boldsymbol{s}_{1i} - J_H\sum_{i}\sum_{\alpha=2}^{3}\boldsymbol{S}_i\cdot\boldsymbol{s}_{\alpha i}. \quad [S1]$$

The three bands $\alpha = 1,2,3$ represent the d_{XY}, d_{XZ}, and d_{YZ} orbitals arranged in a square lattice slightly below the interface. The itinerant electrons interact with a lattice of localized electron spins, believed to reside on d_{XY} orbitals of Ti near the interface layer (3, 4). The index i represents the local moment sites, whose concentration we take as a phenomenological parameter. The spin operators $\boldsymbol{S}_i \equiv \frac{1}{2}d_i^{+}\boldsymbol{\sigma}\,d_i$ represent the local moment spins and $\boldsymbol{s}_i \equiv \frac{1}{2}c^{+}_{\alpha i}\boldsymbol{\sigma}\,c_{\alpha i}$ are the spin operators constructed from the itinerant electrons. Here, $\boldsymbol{\sigma}$ are Pauli matrices acting in the electron spin space, whereas d_i and $c_{\alpha i}$ are two component spinor operators in this space representing the localized and itinerant electrons, respectively. The chemical potential μ sets the density of the itinerant electrons and λ is a Lagrange multiplier that fixes the density of the localized electrons.

The dispersion matrix $\varepsilon(\boldsymbol{k})$ is the same as considered in the supplement to ref. 1.

$$\epsilon(\boldsymbol{k}) = \begin{pmatrix} \frac{k^2}{2m_l} - \Delta_E & 0 & 0 \\ 0 & \frac{k_x^2}{2m_l} + \frac{k_y^2}{2m_h} & -\Delta_d k_x k_y \\ 0 & -\Delta_d k_x k_y & \frac{k_x^2}{2m_h} + \frac{k_y^2}{2m_l} \end{pmatrix},$$

where $m_l = 0.7\ m_e$ and $m_h = 15\ m_e$. In addition to nearest-neighbor hopping, we have included a diagonal hopping term $\Delta_d = m_h^{-1}$ that couples the d_{XZ} and d_{YZ} orbitals. $\Delta_E = 47$ meV is the energy offset of the d_{XY} band. The atomic spin–orbit coupling is described by the local quadratic Hamiltonian

$$\mathcal{H}_{SO} = \Delta_{SO}\sum_{j,\alpha,\alpha'} c^{+}_{\alpha j}\,\boldsymbol{L}_{\alpha\alpha'}\cdot\boldsymbol{\sigma}c_{j\alpha'},$$

where $\boldsymbol{L}_{\alpha\alpha'}$ are the $l = 2$ angular momentum matrices projected to the space of the three t_{2g} orbitals (see also the supporting information in ref. 1). Finally, the coupling to an external in-plane magnetic field is given by the Hamiltonian

$$\mathcal{H}_H = -\mu_B\boldsymbol{H}\cdot\sum_{j} c^{+}_{\alpha j}(\boldsymbol{L}_{\alpha\alpha'}\otimes I + gI\otimes\boldsymbol{\sigma})c_{j\alpha'}.$$

The first term above is the coupling of the magnetic field to the orbital angular momentum, the second is the Zeeman term, I represents a unit matrix either in spin or orbital space, and g is the bare electronic g factor.

To understand the quantum ground states of this model, we use a variational mean-field approximation in the spirit of the standard large N mean-field theory of the Kondo lattice (see for example ref. 5). The variational wavefunction is generated from a quadratic mean-field Hamiltonian

$$\mathcal{H}_{MF} = \mathcal{H}_0 + \sum_{i,\sigma}\left(\chi d^{+}_{\sigma i}c_{\sigma 1 i} + h.c.\right) - \sum_{j}\sum_{\alpha=1}^{3}M_\alpha s_j^x - \sum_{i}M_d S_i^x. \quad [S2]$$

Here, $\mathcal{H}_0$ includes all of the quadratic terms in Eq. **S1**. χ is the singlet hybridization field, which describes collective screening of the moment spins (6). The parameters M_α and M_d account for the induced magnetization on the itinerant bands and the local moments, respectively. We assume $M_2 = M_3$ to preserve orbital symmetry.

We solve for the variational parameters by minimizing the expectation value of the full Hamiltonian (Eq. **S1**) with respect to χ, M_1, M_2, and M_d, where the expectation value is taken with the

ground state of the mean-field Hamiltonian (Eq. **S2**). In other words, we seek the solution of the following set of equations:

$$\frac{\partial\langle\mathcal{H}\rangle}{\partial\chi}=0;\frac{\partial\langle\mathcal{H}\rangle}{\partial M_1}=0;\frac{\partial\langle\mathcal{H}\rangle}{\partial M_2}=0;\frac{\partial\langle\mathcal{H}\rangle}{\partial M_d}=0. \qquad \textbf{[S3]}$$

These equations are supplemented by two additional equations

$$-\frac{\partial\langle\mathcal{H}\rangle}{\partial\mu}=\sum_j\sum_{\alpha=1}^{3}\langle c_{\alpha j}^{+}c_{\alpha j}\rangle=N;\ -\frac{\partial\langle\mathcal{H}\rangle}{\partial\lambda}=\sum_i\langle d_i^{+}d_i\rangle=N_d,$$

which fix the number of itinerant and localized electrons independently.

In the main text, we argued that the diverging critical field obtained from this model (gray line in Fig. 3*C*) is consistent with a transition from a Kondo phase to a magnetically polarized phase. Indeed, the set of variational equations (Eq. **S3**) has two distinct solutions: one where χ is finite which is identified with the Kondo or "heavy liquid" phase, and the other where χ is strictly zero and the moments are fully polarized. The theoretical fit to the critical field presented in Fig. 3*C* is obtained by comparing the energy of these two variational wavefunctions as a function of the applied field H, using $n_d = 2.6\times10^{12}$ cm^{-2}, $J_K =$ 900 meV, and $J_H = 625$ meV. This approach predicts that the transition is of first order, that is, the value of χ at the transition is finite (Fig. S5). Generically this should be expected because both phases do not break any symmetry of the Hamiltonian (Eq. **S1**). However, we point out that large N mean-field theories are known to give spurious first-order transitions.

3. Why d_{XY} Conduction Electrons Couple Antiferromagnetically to Localized Moments Whereas d_{XZ}/d_{YZ} Conduction Electrons Couple Ferromagnetically to Them. To understand why the d_{XY} conduction electrons couple differently to localized moments compared with the d_{XZ}/d_{YZ} , let us consider the on-site Hamiltonian of a single local moment:

$$\mathcal{H}_d=\sum_\alpha\epsilon_\alpha n_\alpha^d+U\sum_\alpha n_{\alpha\uparrow}^d n_{\alpha\downarrow}^d+U'\sum_{\alpha\neq\alpha'}\sum_{\sigma\sigma'}n_{\sigma\sigma}^d n_{\alpha'\sigma'}^d-J\sum_{\alpha\alpha'}\boldsymbol{S}_\alpha\cdot\boldsymbol{S}_{\alpha'}.$$

Here, n_α^d is the density operator of the localized state, ε_α are the single particle energies, U and U' are the inter- and intraorbital Hubbard interactions, respectively, and J is the Hund's rule coupling. The energies ε_α belong to the different orbital states on the moment: ε_1 belongs to the d_{XY} orbital and ε_2, ε_3 are the energies of d_{XZ}, d_{YZ} (Fig. S4*D*). The splitting between these states $\delta = \varepsilon_2 - \varepsilon_1$ is unknown and might be large (3).

The effective magnetic coupling between conduction electrons and the localized moments can be estimated in second-order perturbation theory where the itinerant electron hops into a virtual state on the localized site and back (Fig. S4). The hopping along the z direction of a d_{XY} itinerant electron into a d_{XY} localized state on the moment has a small ("heavy") hopping amplitude, t_h (Fig. S4*A*), resulting in the following hybridization Hamiltonian:

$$\mathcal{H}_{hyb}^{1}=-t_h\sum_i\left(d_{1i}^{+}c_{1i}+h.c.\right).$$

This is exactly the hopping element responsible for the heavy electronic mass in $SrTiO_3$ (STO), and its smallness results from the small overlap of the d_{XY} wavefunctions along the z direction (their lobes are in the XY plane). This process is possible only if the hopping is to a state with spin antiparallel to the spin of the localized moment. The intermediate energy of this second-order process is approximately $U + \varepsilon_1$. Similarly, the localized electron can hop into the conduction band and back with an intermediate energy denominator $\sim \varepsilon_1$; therefore, the coupling is antiferromagnetic (AFM) and is given by (6)

$$J_K\sim t_h^2\left(\frac{1}{U+\epsilon_1}-\frac{1}{\epsilon_1}\right). \qquad \textbf{[S4]}$$

For the d_{XZ}/d_{YZ} conduction electrons one can think of two processes; the first is where the conduction electrons hop into higher unoccupied states at the moment's site with the same orbital symmetry (Fig. S4*B*), which is described by the following hybridization Hamiltonian:

$$\mathcal{H}_{hyb}^{23}=-t_l\sum_i\sum_{\alpha=2}^{3}\left(d_{\alpha i}^{+}c_{\alpha i}+h.c.\right).$$

In this case, electrons with both parallel and antiparallel spin with respect to the spin of the localized moment can hop in. However, due to the Hund's coupling, the hopping to states with parallel spin alignment will have a smaller energy denominator $U' + \varepsilon_2 - J$, compared with hopping to states with antiparallel spin alignment, whose energy denominator is $U' + \varepsilon_2 + J$. The resulting effective coupling between the d_{XZ}, d_{YZ} itinerant electrons and the localized moment is therefore ferromagnetic and is given by

$$J_H\sim t_l^2\left(\frac{1}{U'+\epsilon_2-J}-\frac{1}{U'+\epsilon_2+J}\right). \qquad \textbf{[S5]}$$

The d_{XZ}/d_{YZ} itinerant electrons can also hop to a d_{XY} state on the localized site through a next-nearest-neighbor diagonal hopping processes with amplitude t_d (Fig. S4*C*)

$$\tilde{\mathcal{H}}_{hyb}^{23}=-t_d\sum_{<ii'>}\sum_{\alpha=2}^{3}\left(\eta_{ii'}^{\alpha}\,d_{\alpha i}^{+}c_{\alpha i'}+h.c.\right),$$

where $\eta_{ii'}^{\alpha}=\mathrm{sign}(i-i')$ and is nonzero only if $i - i'$ is along y and $\alpha = 2$ or along x and $\alpha = 3$. This hybridization is the same as the diagonal hopping which hybridizes the d_{XZ} and d_{YZ} in the plane (see the supplement to ref. 1). Just as the process described in Fig. S4*A*, this process too will give rise to an antiferromagnetic superexchange coupling. However, this coupling is negligible compared with the ferromagnetic (FM) coupling for two reasons. The first is that the hopping processes from the two sides of the moment have opposite signs and therefore interfere destructively. The second is that the hopping element t_d is an order of magnitude smaller than the light hopping t_l responsible for the FM coupling in Fig. S4*B*.

4. Detailed Gate Dependence of Hall Resistivity for Sample in Main Text. In Fig. 4*B* we showed, as a 3D plot, the dependence of the anomalous Hall effect (AHE), ρ_{XY}^{AHE}, in the density–field plane after subtracting out the low-field slope from the measured antisymmetric component of the transverse resistivity ρ_{XY}^{A}. The AHE thus obtained, $\rho_{XY}^{AHE}=\rho_{XY}^{A}-H_{tot}\cdot d\rho_{XY}^{A}/dH_{tot}$, was negligibly small for low fields but showed a step that developed rapidly above a critical field. Here, we show the raw dataset of ρ_{XY}^{A} as a function of the total field H_{tot} and density without the subtraction procedure.

The various gate voltages used to tune the density correspond to the individual line traces in Fig. S3. At the highest gate voltages used so that the carrier density was well above the Lifshitz critical density, the ρ_{XY}^{A} trace (red) is linear in H_{tot} at low fields. Around $H_C^{\parallel}=2.5T$ it rises sharply, and at higher fields it once again stabilizes on a gradual linear dependence on H_{tot}. The slope at

these higher fields is comparable, yet slightly smaller than that at low fields. As the gate voltage is decreased and the density is lowered in the system, two changes are immediately apparent in the shape of the line trace: whereas the low-field slope remains almost fixed, the step in ρ_{XY}^{A} occurs at a larger $H_C^{||}$ and the size of the step is also larger. At fields $H_{tot} > H_C^{||}$, once again the Hall resistivity ρ_{XY}^{A} settles on a slope that is slightly smaller compared with its low-field value. These trends progressively continue as the gate voltage is decreased further (red through orange, green, and cyan traces), until $H_C^{||} > 14T$ and the step lies outside our maximum applied field, leaving only the initial rise of the step to be seen (blue to purple traces). Finally, the density falls just below the critical density (brown and black traces) and ρ_{XY}^{A} remains completely linear up to the highest field. Thus, the buildup of the AHE at $H_C^{||}$ and the divergence of this critical field at the Lifshitz density, characteristic features of the $LaAlO_3$ (LAO)/STO system reported in the main text, are also clearly visible in the raw data.

A notable feature common to all of the traces is that they ride on a slope that has approximately the same value for all of them. This observation can be traced to the fact that the slope of the Hall resistivity, i.e., the Hall coefficient, at low values of the perpendicular field is inversely proportional to the number of high-mobility d_{XY} carriers (1). Because the field is applied almost in-plane, its perpendicular component is quite small even up to the maximum applied value of $H_{tot} = 14T$. The overall slope of the traces shown in Fig. S3 is therefore determined by the density of carriers in the d_{XY} band, which remains fixed at the critical density for all densities of the total number of carriers exceeding this value (red to purple traces). In fact, because the gate is not tuned significantly below the critical value, even the lowest density (brown and black) traces shown in Fig. S3 do not have a significantly larger slope compared with the high-density traces.

5. Phase Diagram for a 10 unit cells (uc) Sample and Another 6-uc Device. In the main text, we presented AMR and AHE data from a 6-uc sample grown at T_{growth}=800 °C. Here, we show similar results obtained in a 10-uc sample, grown at a different temperature, T_{growth} = 650 °C. Specifically, we show that the density dependence of the critical field extracted from AMR and AHE measurements across samples is similar.

Fig. S1*A* shows the critical field $H_C^{||}$ extracted from the position of the step in AHE measurements on a high-mobility 10-uc sample. In these AHE measurements, the field was applied at an angle of $\theta = 0.7°$ to the plane of the interface. We find that $H_C^{||}$ increases as the LAO/STO system is progressively depleted. Plotting the reciprocal of this field, $1/H_C^{||}$, we find that at low densities the data points collapse onto a single line that extrapolates to zero in the vicinity of the critical density associated with the Lifshitz transition (Fig. S1*B*). Exactly the same trends are also seen from AMR measurements on another Hall device on the same sample reported in the main text: $H_C^{||}$ appears to diverge at the critical density (Fig. S1 *C* and *D*). Thus, as shown in the main text, not only is the critical field determined from AMR and AHE similar (Figs. 3*A* and 4*B*), but this observation holds even across samples, where $H_C^{||}$ appears to be divergent in the vicinity of the Lifshitz transition characteristic for each sample.

6. Methods. ***Sample fabrication.*** As detailed in earlier work (7), films were grown on TiO_2-terminated (001) $SrTiO_3$ single crystals of dimensions 5 mm × 5 mm by pulsed laser deposition in ~10^{-4} mbar of O_2. The repetition rate of the laser was 1 Hz, with the fluence of each pulse being 0.6 J cm^{-2}. The film growth was monitored in situ using reflection high-energy electron diffraction. The 6-uc (/10-uc) sample was grown at T= 800 °C (T= 650 °C). After growth, the samples were annealed in 200 mbar of O_2 at about 600 °C (/530 °C) for 1 h and cooled to room temperature in the same oxygen pressure. Hall bars were photolithographically patterned and the sample was ultrasonically bonded using Al wire.

Measurements. We used back-gated Hall bars with widths ranging from 100 to 500 um, oriented along the (100) crystallographic direction. Current (amplitude of 46 nA at frequencies ranging from dc to 13 Hz) was passed along this direction, and the longitudinal and transverse resistivities (ρ_{XX} and ρ_{XY}) were measured while rotating the sample in a magnetic field applied in the plane of the interface at temperatures of $T = 2$ K. The absence of nonlinear effects was confirmed by ensuring similar data were measured despite lowering the amplitude of the current by an order of magnitude. The possibility of nonequilibrium effects was ruled out by testing different durations of wait time after perturbing the system and subsequently using, in the data acquisition, a wait time for which the system had relaxed.

1. Joshua A, Pecker S, Ruhman J, Altman E, Ilani S (2012) A universal critical density underlying the physics of electrons at the $LaAlO_3/SrTiO_3$ interface. *Nat Commun* 3:1129.
2. Ben Shalom M, et al. (2009) Anisotropic magnetotransport at the $SrTiO_3/LaAlO_3$ interface. *Phys Rev B* 80(14):140403(R).
3. Pentcheva R, Pickett WE (2006) Charge localization or itineracy at LaAlO3/SrTiO3 interfaces: Hole polarons, oxygen vacancies, and mobile electrons. *Phys Rev B* 74(3):035112.
4. Michaeli K, Potter AC, Lee PA (2012) Superconducting and ferromagnetic phases in SrTiO3/LaAlO3 oxide interface structures: Possibility of finite momentum pairing. *Phys Rev Lett* 108(11):117003.
5. Coleman P (2007) *Handbook of Magnetism and Advanced Magnetic Materials*, eds Kronmuller H, Parkin S (Wiley, Singapore), Vol 1, p 95.
6. Hewson AC (1997) *The Kondo Problem to Heavy Fermions* (Cambridge Univ Press, Cambridge, UK).
7. Caviglia AD, et al. (2008) Electric field control of the LaAlO3/SrTiO3 interface ground state. *Nature* 456:624–627.

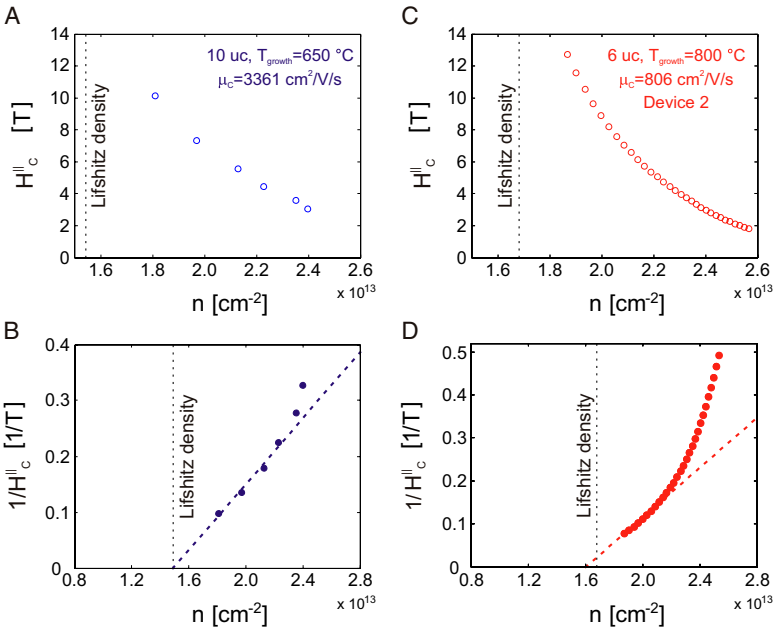

Fig. S1. Phase diagram for additional 10-uc sample and another 6-uc device. (*A*) $H_C^{\parallel}$ and (*B*) $1/H_C^{\parallel}$ extracted from anomalous Hall effect measurements of a 10-uc sample, as a function of total carrier density. (*C*) $H_C^{\parallel}$ and (*D*) $1/H_C^{\parallel}$ from AMR of another device on the 6-uc sample of the main text, vs. density.

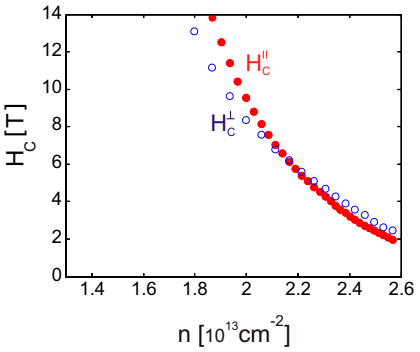

Fig. S2. Comparison of parallel and perpendicular critical fields. $H_C^{\parallel}$ taken from Fig. 3*C* (solid red circles) and scaling perpendicular field (blue circles), reported previously (1), bear remarkable similarity both in their magnitude and in their trend as a function of total carrier density in the system.

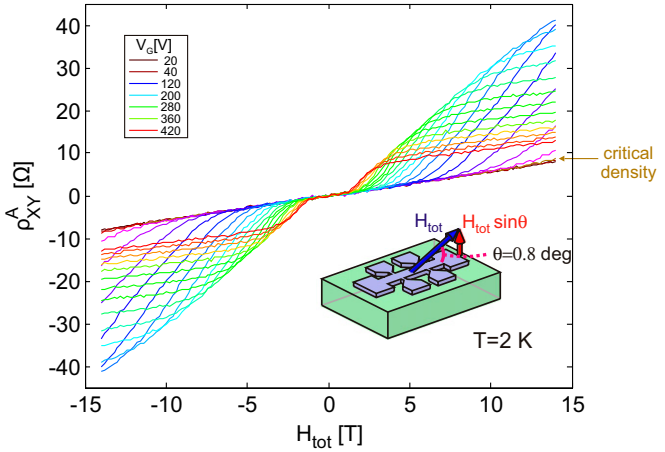

Fig. S3. Hall resistance ρ_{XY}^{A} as a function of nearly in-plane field H_{tot} for various gate voltages. At densities much above the Lifshitz value (high gate voltages), the traces have a step at a critical field. The traces become completely linear as the density is tuned from above to below the Lifshitz critical density (low gate voltages). (*Inset*) Geometry of the measurement.

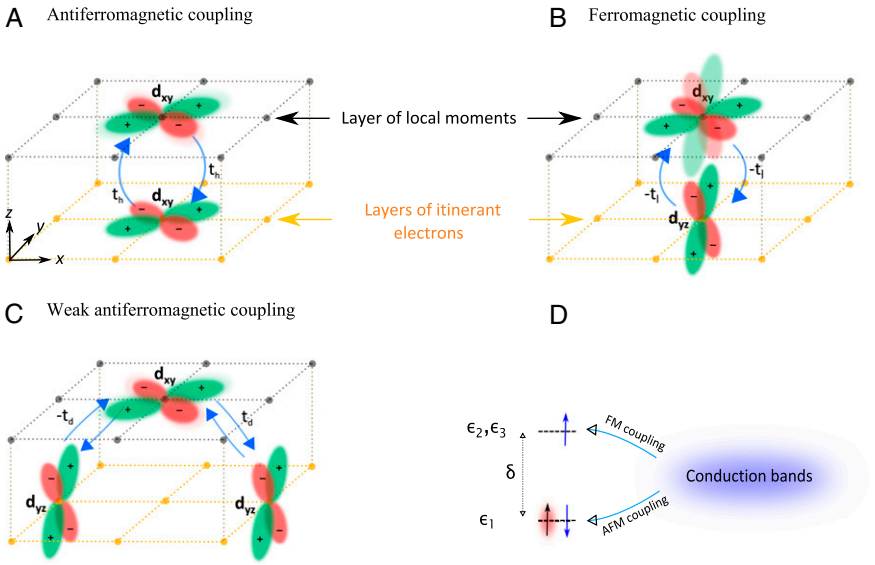

Fig. S4. Schematic representation of the hopping processes between localized and itinerant electronic states. The first few TiO_2 layers are occupied by the localized states of d_{XY} symmetry whereas subsequent TiO_2 layers, further away from the interface, hold itinerant electrons that can be of either d_{XY}, d_{XZ}, or d_{YZ} symmetry. (*A*) Hopping between the d_{XY} itinerant electron and a d_{XY} localized state. This process has a small heavy hopping amplitude t_h, because the lobes of the wavefunctions are perpendicular to the hopping direction. (*B*) Hopping between the d_{YZ} itinerant electron and the unoccupied d_{YZ} state on the moment site. This process has a large "light" amplitude t_l, because the lobes of the wavefunctions are pointing in the hopping direction. (*C*) Hopping between the d_{YZ} itinerant electrons and the d_{XY} localized state is only allowed through a next-nearest-neighbor diagonal hopping process (1), with amplitude t_d that is comparable to the heavy hopping amplitude. (*D*) Resulting exchange coupling. The energy diagram of the moment state is shown, whose occupied d_{XY} state is lower in energy by δ compared with the unoccupied d_{XZ} and d_{YZ} states. The process in *A* gives an AFM superexchange between itinerant d_{XY} electrons and the localized moment. The virtual hopping process in *B*, together with local Hund's coupling on the localized state, yields an effective FM coupling between d_{XZ} and d_{YZ} electrons and the localized moment. The latter process has a large energy denominator (δ), but on the other hand involves much larger hopping amplitude $t_l \gg t_h, t_d$. Because the exchange terms are quadratic in the hopping amplitudes, this term would be quite large.

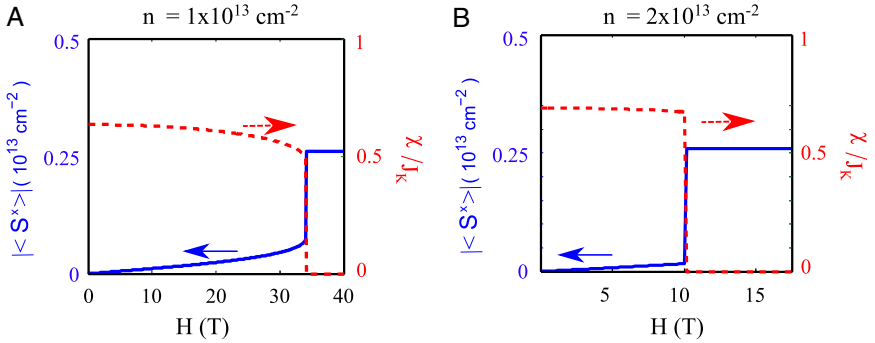

Fig. S5. Magnetic-field–driven transition from "heavy liquid" phase to polarized phase, given by the variational calculation. The average magnetization of the moment band $|\langle S^x \rangle|$ and the singlet hybridization χ/J_K plotted as a function of the applied magnetic field H for (*A*) itinerant electron density $n = 1 \times 10^{13}$ cm^{-2} (below the Lifshitz density) and (*B*) $n = 2 \times 10^{13}$ cm^{-2} (above the Lifshitz density). At a critical value $H = H_c$, χ jumps to zero whereas $\langle S^x \rangle$ jumps to its maximum value. For both *A* and *B*, the parameters are $n_d = 2.6 \times 10^{12}$ cm^{-2}, $J_K = 900$ meV, and $J_H = 625$ meV.